Photoluminescence System for Detecting Sub-Bandgap Photon Emission in Silicon

Undergraduate Honors Thesis

Presented in Partial Fulfillment of the Requirements for Graduation with Honors Research Distinction in Electrical and Computer Engineering at The Ohio State University

By

Ryan J. Patton

November 2015

Advisor

Professor Ronald M. Reano

The Ohio State University

Department of Electrical and Computer Engineering

Abstract

Electro-optical systems are essential for the next generation of communication networks. As photonic devices become smaller, one sees a future where microelectronic and optical technologies are completely integrated. This requires a unified material platform, and one of the best candidates is silicon. Silicon is already widely used in the microelectronics industry, and several chip scale photonic devices have been demonstrated using Silicon on Insulator (SOI) technology. Unfortunately, silicon lacks a native light source due to its indirect bandgap. An on chip light source is necessary to fully realize the potential of densely integrated photonic circuits. Recent research has explored sub-bandgap luminescence in silicon as a possible solution. The inherently low power at this stage of research requires efficient characterization techniques. Reported here is the development of a photoluminescence experimental system for detecting sub-bandgap light emission in silicon. The system is used to measure sub-bandgap luminescence from research level samples.

Acknowledgments

First and foremost I want to thank Professor Ronald M. Reano. As an instructor, project advisor, and mentor, he has helped me to grow immensely in knowledge and passion for engineering. Our discussions kept me curious and motivated throughout the project. I would also like to thank Michael Wood, for welcoming me into his PhD work, and taking the time to educate and encourage me over many months. Additionally, I want to thank Tyler Nagy and Justin Burr for their valuable discussions, and for introducing me to the myriad of tools at my disposal in the lab. Finally, I want to thank Professor Roberto C. Myers for taking the time to show me his laboratory, discussing the initial project, and ultimately sitting on my defense committee.

This research was supported in part by the College of Engineering Undergraduate Research Scholarship, and the Undergraduate Research Office Honors Summer Research Scholarship.

Table of Contents

1. Introduction 1

1.1 Background 1

1.2 Broader Impacts 2

1.3 Objectives 2

1.4 Literature Review 2

2. Design 4

2.1 Overview 4

2.2.1 Laser Diode 5

2.2.2 Optical Fiber 6

2.2.3 Collimators 6

2.2.4 Dichroic Mirrors and Optical Filters 7

2.2.5 Digital Microscope and Objective 9

2.2.6 Monochromator and CCD 10

2.3 Measurement Parameters 12

3. System Calibration 13

3.1 Alignment 13

3.2 Characterization 15

3.2.1 Infrared Laser Transmission Tests 15

3.2.2 Calculation of Light Collection Efficiency 18

3.2.3 Calculation of Incident Power Density 20

3.2.4 Sources of Noise 22

4. Measurements and Discussion 24

4.1 Laser Noise and Ghosting 24

4.3 Grating Comparison 28

4.4 Sub-Bandgap Photoluminescence from SOI 29

6. Conclusion 31

7. Future Work 32

8. References 33

Appendix 35

Table of Figures

Figure 1: Silicon Energy Diagram 1
Figure 2: Basic Photoluminescence Setup [3] 3
Figure 3: Photoluminescence System Diagram 4
Figure 4: Measured Laser Power 5
Figure 5: Fiber Numerical Aperture [17] 6
Figure 6: (Left) Percent reflection of the F280FC-B Collimator. (Right) Beam Divergence Angle [14] 7
Figure 7: Longpass Filter Optical Density 8
Figure 8: Laser Path Optical Density 9
Figure 9: Infinity Corrected Imaging System [18] 9
Figure 10: Monochromator and CCD Diagram 10
Figure 11: Grating Efficiency for the Linear Polarization States (TE and TM). [15] 11
Figure 12: 10 Second Dark Signal 12
Figure 13: Misalignment Cases 13
Figure 15: Alignment Setup 1 14
Figure 15: Alignment Setup 2 14
Figure 16: (Left) Test 1 Setup. (Right) Measured Loss from Collimator to Sample 16
Figure 17: (Left) Test 2 setup. (Right) Measured Field of View Loss 17
Figure 18: (Left) Spectra of the IR Laser. (Right) Total Laser Power Reaching the CCD 17
Figure 19: Measured System Loss 18
Figure 20: Radiating Point in the Sample. Solid Angles **Ω1** and **Ω2** Describe Acceptance Cone of the Objective 19
Figure 21: Gaussian Beam Propagation 21
Figure 22: (Left) Imaged Laser Spot. (Right) Two Term Gaussian Fit to Image Intensity 22
Figure 23: (Left) Laser Line Spectrum. (Middle) Near IR Spectrum – Laser Off. (Right) Near IR Spectrum – Laser On. 24
Figure 24: Example Laser Spectrum 24
Figure 25: Fundamental and Second Order Diffraction of Laser Light 25
Figure 26: Grating Ghosts 25
Figure 27: Silicon Band-Edge PL with Variable Integration Time 26

Figure 28: Silicon Band-Edge PL with 30 s Integration at 103 mA 27
Figure 29: Measured Detector Response 27
Figure 30: Silicon Band-PL after Data Correction 28
Figure 31: Silicon Band-Edge PL vs Grating 29
Figure 32: SOI Sample with Hydrogen Plasma Treatment 30
Figure 33: SOI Sub-Bandgap PL Comparison 30
Figure 34: PL from hydrogen plasma treated SOI reported in [13] 31
Figure 35: Parts List 35

1. Introduction

1.1 Background

Nano-scale integrated optical technologies are essential for realizing next generation high speed and high bandwidth communication networks. The silicon material platform, which has been the cornerstone of microelectronics for decades, is a strong candidate for integrated photonic devices. The high refractive index contrast between Si and SiO_2 or other cladding materials allows for strong light confinement and low loss propagation in silicon. Additionally, knowledge from the microelectronics industry can be directly applied to new silicon photonics research. The capabilities of silicon photonics have expanded rapidly to include high-speed modulators, photodetectors, biological sensors, and low loss optical interconnects for telecommunication systems.

One major drawback is that silicon's crystal structure results in an indirect bandgap. This means a phonon (vibrational energy packet) is required for radiative recombination, which makes the process unlikely compared to non-radiative recombination. Thus room temperature band-edge light emission (luminescence) is an inherently inefficient process in silicon. Typical efficiencies are on the order of 10^{-6} to 10^{-7} [1]. Additionally, any emitted light will be near the bandgap energy and prone to absorption, which is not suitable for on chip routing of optical signals. However, light below the bandgap energy is not readily absorbed, therefore recent research has focused on enhancing sub-bandgap luminescence in silicon. Sub-bandgap light can be generated when carriers recombine through defect states as shown in Figure 1. If carriers are excited electrically,

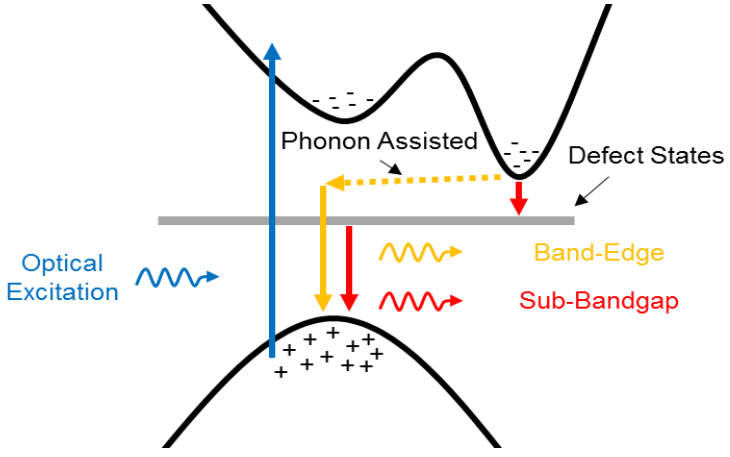

Figure 1: Silicon Energy Diagram

the emitted light is called electroluminescence (EL). However the introduction of electrical contacts adds complexity to the fabrication process, and can impact the phenomenon under investigation. Thus optical excitation, typically with a laser, is the preferred method. The emitted light is accordingly called photoluminescence (PL).

The motivation for this research comes from recent work at the University of St. Andrews. They report that treating silicon on insulator (SOI) with hydrogen plasma enhances the sub-bandgap luminescence [2]. The emission was further enhanced by coupling the light to a nanocavity. Our group is interested in building on this work by investigating different plasma treatments and cavity designs. This requires a sensitive and robust photoluminescence system specifically tailored for detecting sub-bandgap light emission in silicon nanocavities.

1.2 Broader Impacts

The technology boom of the last few decades has radically changed how people learn and communicate. There is an ever increasing demand for more data and more processing power. Achieving low power and densely integrated photonic devices will be necessary to keep up with data demand. Current technology relies on bonding III-V materials such as GaAs onto silicon to fabricate light sources. The added cost and fabrication complexity stunts wide spread adoption and manufacturing of nano-scale photonic devices. An integrated silicon light source could provide a low cost solution on a material platform which is already widely used in industry. This would facilitate the transition of optical technologies from the laboratory to the consumer.

1.3 Objectives

The first research objective is to design and build a photoluminescence system which can detect sub-bandgap luminescence from silicon nanocavities. The design must focus the laser to a small enough spot for targeting nano-cavities, and be able to control the laser position on the sample. The second objective is to conduct measurements and analyze the data to motivate the next stage of research.

1.4 Literature Review

Photoluminescence is commonly used in research to study material properties, especially near the surface. In [3], Gfroerer outlines a basic PL setup as shown in Figure 2. It consist of an optical pump (laser), the sample under investigation, collection optics, and a spectrometer.

Gfroerer highlights the simplicity and versatility of using photoluminescence to study material surface properties. However he also discusses the difficulty associated with investing materials with poor luminescence efficiency. Thus indicating that high sensitivity will be crucial.

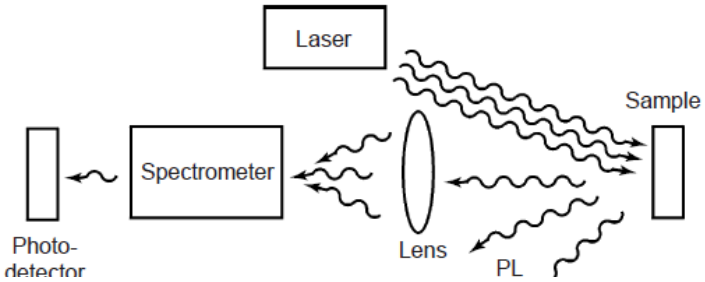

Figure 2: Basic Photoluminescence Setup [3]

The group in [4] studies silicon nanocrystals, which also exhibit an indirect bandgap. Low temperature measurements are used to enhance the signal and gain insight into the material properties. Their setup includes a liquid nitrogen cooled charge coupled device (CCD) for detection, a grating imaging spectrometer, and a high numerical aperture (NA) objective. NA quantifies the light gathering power of the optic, and typically varies between 0 and 1. The laser intensity was $1W/cm^2$ at 325nm, and incident at a grazing angle between the sample and the objective. Their collection time for each measurement was about 30 minutes to achieve a suitable signal to noise ratio (SNR). A study of silicon photonic crystal nanocavities (PhCs) [5] incorporates polarization control. The incident laser light is linearly polarized, and the collected light is analyzed by a crossed polarizer. Both the excitation and emission are collinear, passing through the same objective. When focused, the laser spot is 2μm in diameter.

We are interested in developing a light source which can operate at room temperature, thus low temperature measurements are not be especially valuable. The defects are not expected to be polarization sensitive, and attenuating the laser via polarization is undesirable. A microscope objective will be necessary to collect the emitted light. The collinear approach minimizes the number of required optical elements which reduces potential alignment errors. Video feedback will be required to accurately position the laser onto the nanocavities. A fiber coupled output will allow the light to be analyzed by different detectors, minimize stray light, and simplify system characterization. However it will require precise alignment capabilities such as translation and rotation control to couple the PL to the fiber.

2. Design

2.1 Overview

A basic system diagram is shown in Figure 3. The components used will be explained in detail in the following sections. There are three optical paths: excitation, photoluminescence, and imaging. All three are focused by the same objective lens. The beams are combined or separated using dichroic mirrors. Collimators are used to couple the excitation and emission light between fiber and free-space. The digital microscope images the sample, and displays an image of the surface on the computer screen. The emitted photoluminescence is guided by the fiber to a monochromator and CCD detector which is also controlled by the computer. Optical filters prevent unwanted light from entering the detector. Both collimators are mounted on XY

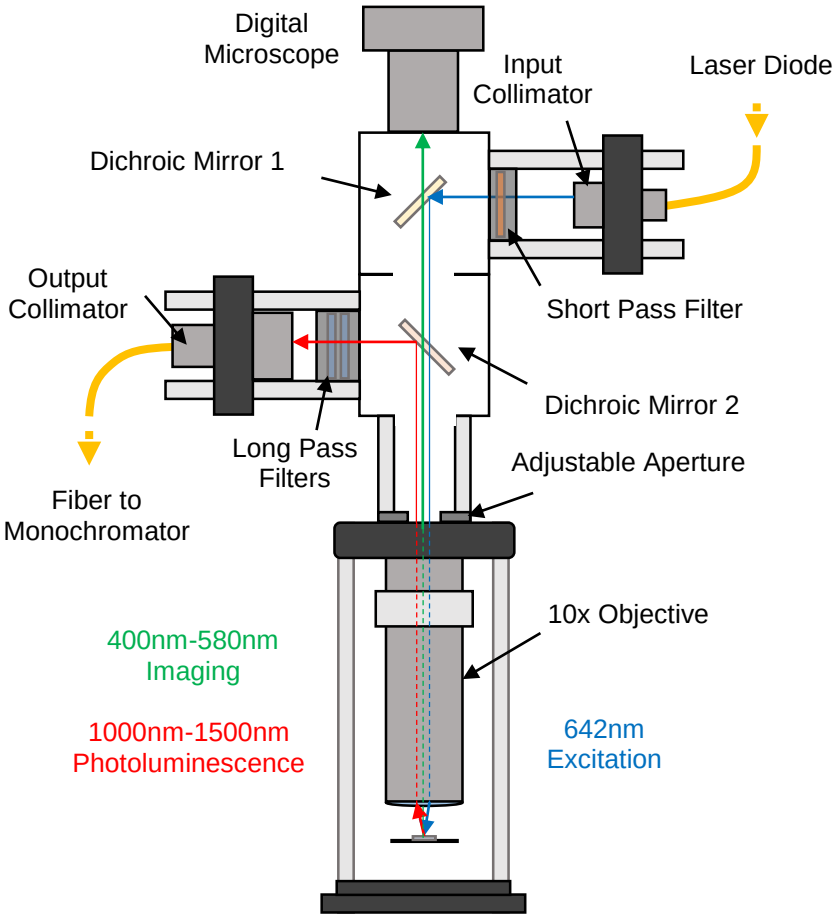

Figure 3: Photoluminescence System Diagram

translation stages, and both mirrors are mounted on precision rotation stages with fine tip, tilt, and height control. The sample is placed on a platform with XYZ translation control.

2.2 Components

A complete list of parts is included in the appendix. Major components are detailed below.

2.2.1 Laser Diode

The pump source is a 642 nm fiber coupled laser diode from Thorlabs. The nominal operating power is 20 mW at 103 mA driving current and 2.41 V forward voltage. The wavelength corresponds to 1.93 eV which is greater than silicon's 1.1 eV bandgap. Thus the photons have enough energy to excite carriers for photoluminescence. The laser diode is housed in an ILX Lightwave mount, which contains thermoelectric coolers (TECs) and a monitoring thermistor. The laser is powered by an ILX precision current source, and the TECs are connected to an ILX thermoelectric temperature controller. The current and temperature controllers are necessary to maintain the laser's power and spectrum during a PL measurement. A plot of the measured power vs. current is shown in Figure 4. The measurement was taken by connecting the fiber directly to a Newport 818-SL photo detector

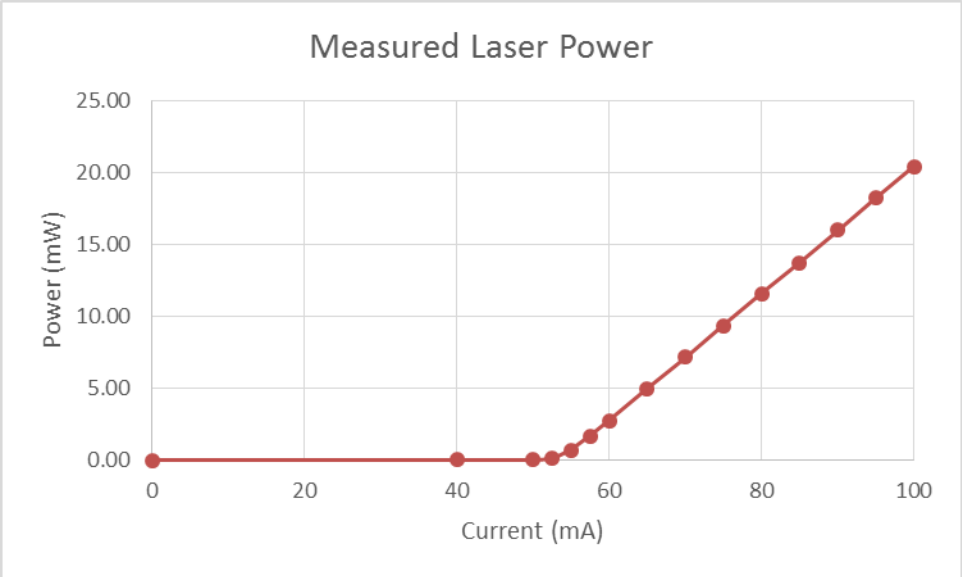

Figure 4: Measured Laser Power

The Occupational Safety and Health Administration reports the Max Permissible Exposure (MPE) at 647 nm as 2.5 mW/cm^2 for 0.25 seconds [6]. As discussed in section 2.2.3 below, the expected beam diameter is 3.4 mm. The max power density is calculated as:

$$\Phi = \frac{20 \text{ mw}}{\pi \left(\frac{3.4}{2} \text{ cm}\right)^2} = 220 \text{ mW/cm}^2$$

This is well above the MPE. Viewing the laser beam from an unintentional reflection, even for a fraction of a second, can result in permanent retina damage. To provide adequate protection, laser safety glasses were purchased which provide 38 dB of attenuation at 640 nm. This reduces the maximum power density to 0.035 mW/cm^2, which safely below the MPE.

2.2.2 Optical Fiber

Fiber optic cable confines light to a silica waveguide, and is used in the lab to route light between different devices. When coupling light between fiber and free space, it is important to know the fiber's numerical aperture (NA). As shown in Figure 5 below, the NA determines the

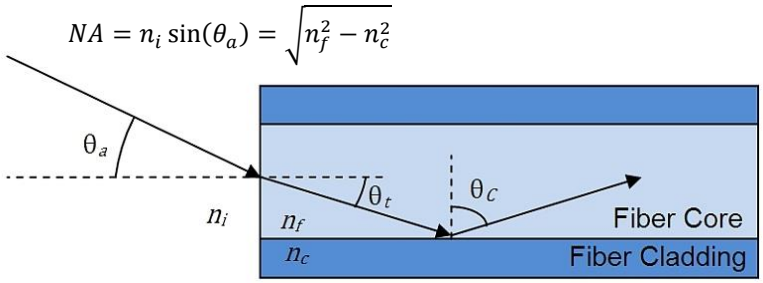

Figure 5: Fiber Numerical Aperture [17]

maximum angle of light accepted or emitted by the fiber. There are two fibers used in the system. The first is the SM600 from Thorlabs with 0.12 NA, which connects the laser diode to the input collimator. The second fiber connects the output collimator to the monochromator. To maximize the collection efficiency, the fiber was chosen to have the largest diameter that could be connected to the collimator. The GIF625 fiber purchased from Thorlabs has a 62.5 μm core diameter, and 0.275 NA. The attenuation is under 0.6 dB/km at 1300nm, resulting in negligible loss for the PL signals.

2.2.3 Collimators

A collimator package consists of one or more lenses, and a fiber connector. It is designed such that the fiber tip sits at the focal point, and the rays exiting the collimator are nearly parallel. The focal length is optimized for a set operating wavelength, and shifts as a function of wavelength offset. Many collimators also employ an anti-reflection coating to maximize transmission at the design wavelength. The F280FC-B collimator couples the laser to free space, and is designed to produce a Gaussian beam with a 3.4mm diameter and 0.014° divergence angle at 633nm center

wavelength. The percent reflection and divergence angle are given as a function of wavelength in Figure 6 below. From Figure 6, 642 nm is still well within the operating limits of the collimator.

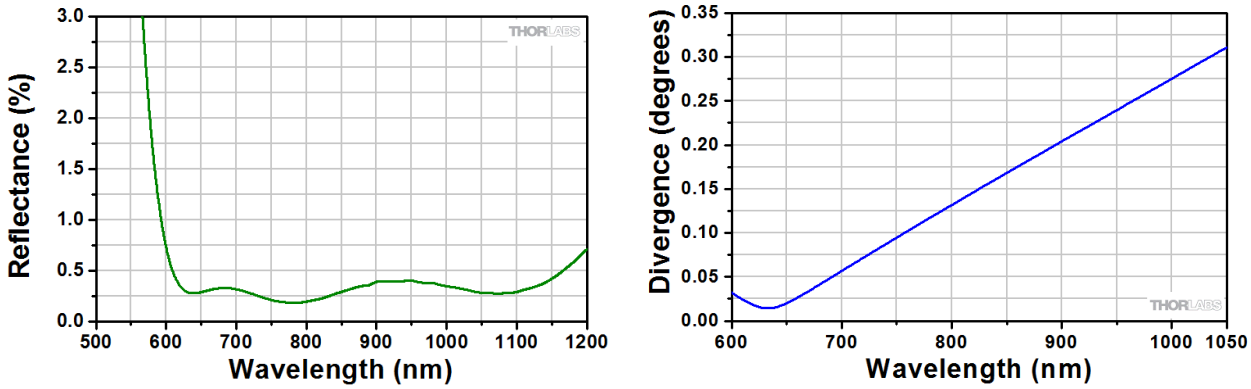

Figure 6: (Left) Percent reflection of the F280FC-B Collimator. (Right) Beam Divergence Angle [14]

The emitted photoluminescence is collected by an F810APC-1550 collimator with 0.24 NA. Parallel rays entering the collimator are focused onto the fiber core.

2.2.4 Dichroic Mirrors and Optical Filters

Dichroic mirrors are reflective for one set of wavelengths, and transparent for another. Thus they are often employed as wavelength selective beamspliters, allowing beams of different wavelengths to be combined or separated. In contrast, optical filters are only rated for transmission, and cannot be used as beamspliters. However, they are able to achieve much greater attenuation of unwanted wavelengths when compared to dichroic mirrors. Thus filters are often described by Optical Density: $OD = -\log(T_{\%}/100)$. Both dichroic mirrors and optical filters are typically denoted as longpass or shortpass with a specific cutoff wavelength, which describes the set of wavelengths with high transmission efficiency through the optic. Examining Figure 3 above, dichroic mirror 1 is reflecting the laser (642nm), and transmitting the sample image. The mirror used is a short pass with a 600 nm cutoff. The second mirror is also short pass, but with a 1000 nm cutoff. It is transparent for the laser and image, but reflective for the emitted photoluminescence.

As discussed in the measurements section below, it is crucial that unwanted light be blocked from entering the detector. Otherwise it is extremely difficult to obtain accurate data. In

the first design iteration, there was no short pass filter in front of the laser, and there was a single long pass filter at the output. While the original filter had a 665nm cutoff, and 0.42% transmission at 640nm, Figure 7 below shows that the filter doesn't reach full attenuation until around 625nm. The 2.4 OD at 640nm was not enough to attenuate the laser power below the noise floor.

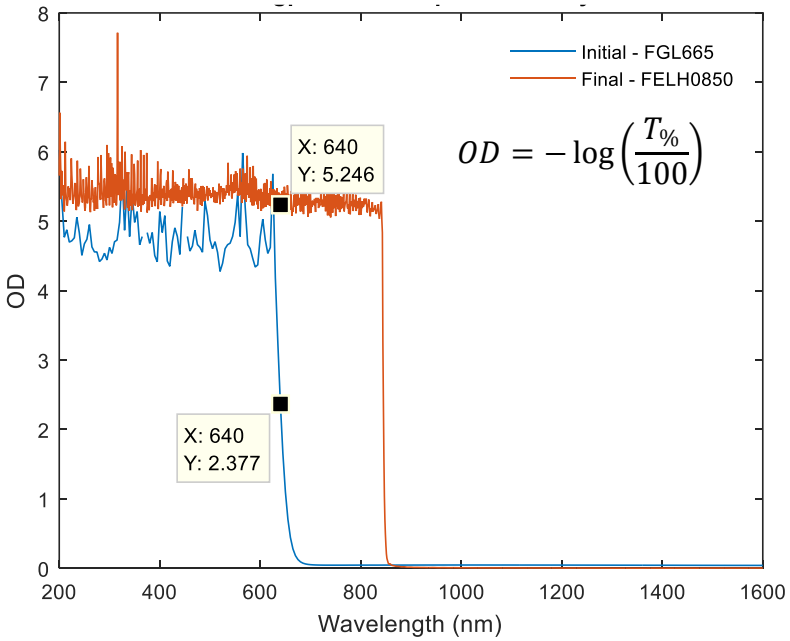

Figure 7: Longpass Filter Optical Density

The first filter was replaced by two high performance longpass filters. An additional short pass filter was placed in front of the laser to reject amplified spontaneous emission (ASE) noise generated between 800nm-1600nm. ASE noise is discussed further in section 3.2.4. The total attenuation provided by the three filters is shown in Figure 8 below. Note that the 10.5 OD is due to the longpass filters, which are not encountered until after the laser has excited the sample. Thus the sample receives full laser power. Similarly the constant 5.5 OD from 850nm to 1600nm is due to the short pass filter placed directly after the laser. Therefore the sub-bandgap PL from the sample is not attenuated.

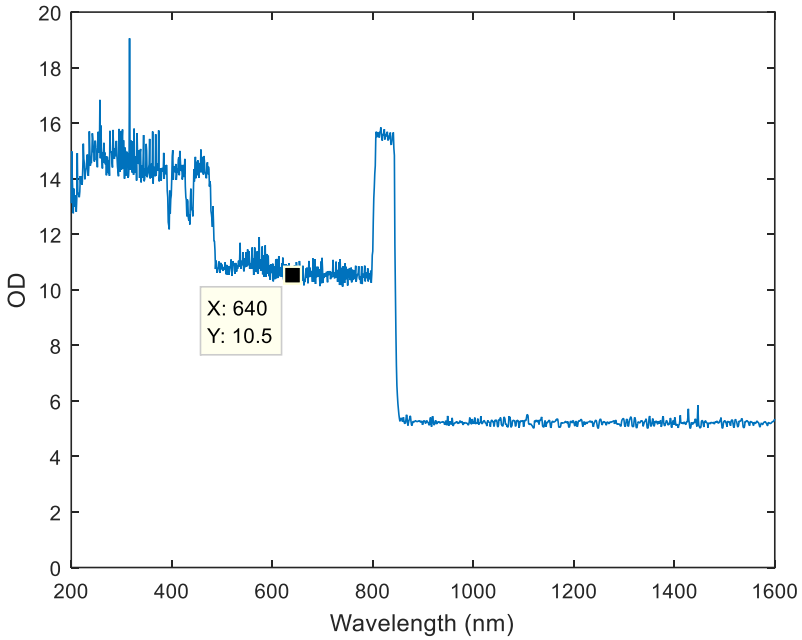

Figure 8: Laser Path Optical Density

2.2.5 Digital Microscope and Objective

The imaging components are from Caltex Systems and include a 2.0 mega pixel digital camera, coaxial illumination from a halogen lamp, five detent variable zoom (30x-200x), and a 10x objective which extends the zoom to 300x-2,000x. The components were originally configured in a single optical stack, and connected by proprietary fittings. The microscope uses an infinity corrected design as shown in Figure 9. Thus the distance between the objective and

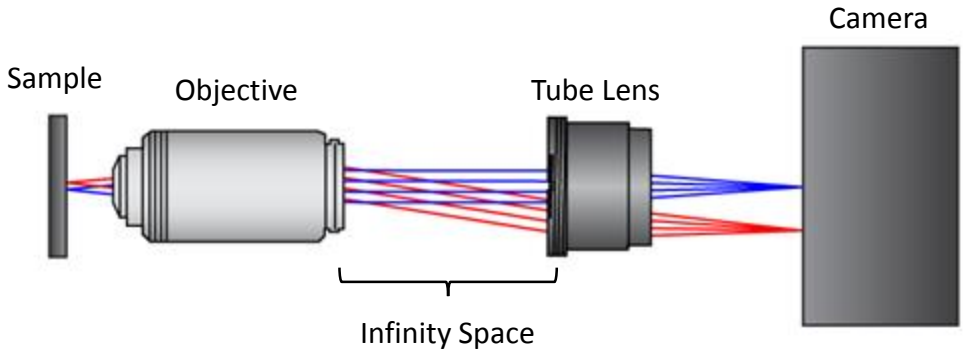

Figure 9: Infinity Corrected Imaging System [18]

tube lens can be extended without distorting the image. This provides space to add additional optics such as the dichroic mirrors. Custom fittings were designed and machined so that the objective and camera could be mounted to the PL system independently. Mechanical drawings of the fittings are provided in the appendix.

2.2.6 Monochromator and CCD

A diagram of the monochromator is shown in Figure 10 below. The fiber from the output collimator in Figure 3 is connected to the monochromator entrance. The lenses focus the light through an adjustable entrance slit, and onto a diffraction grating, which separates the light into its constituent wavelengths. A subset of those wavelengths are incident on the InGaAs CCD detector. The grating is mounted on a rating turret, which allows measurement over a large range of wavelengths. The Horiba iHR550 monochromator contains three different gratings [7] listed below:

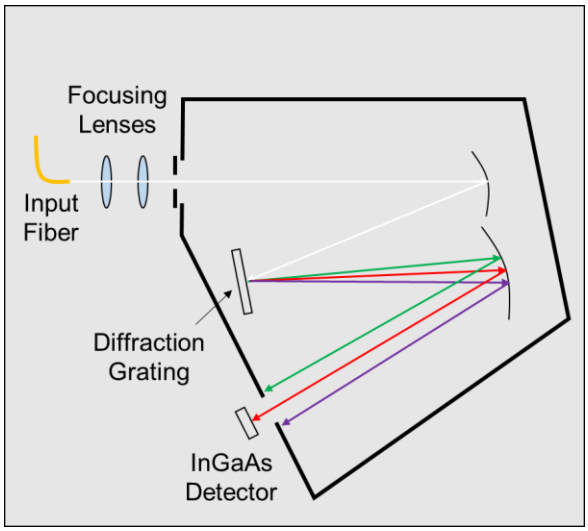

Figure 10: Monochromator and CCD Diagram

Groove Density (G/mm)	900	950	600
Blaze Wavelength (nm)	1500	900	1500

In general a grating is described by the expression [8]:

$$\sin(\theta_i) + \sin(\theta_d) = kn\lambda$$

Where θ_i, θ_d are the incident and diffracted angles, k is the integer diffraction order, and n is the groove density. Because the equation is satisfied for integer multiples of $n\lambda$, short wavelength signals will produce higher order diffractions that can be measured when scanning longer wavelengths. For example, the laser at 642nm will also produce peaks in the data at 1284nm, 1926nm, and so on. The spectral resolution is proportional to the groove density, meaning a higher

density causes the diffracted wavelengths to be more spread out in space, which makes finer spectral features easier to identify. However, this results in lower power per unit area, and therefore decreased sensitivity. Blazed gratings are designed to concentrate a region of the spectrum into a desired diffraction order. The greatest efficiency occurs at the blaze wavelength. For PL measurements, the 600 G/mm grating was chosen because its blaze wavelength is near silicon's sub-bandgap spectral region, and it provides more sensitivity than the 900 G/mm grating because of the lower density. The grating's efficiency curve is given in Figure 11 below. The input is expected to be unpolarized, so the efficiency will be an average of the two curves.

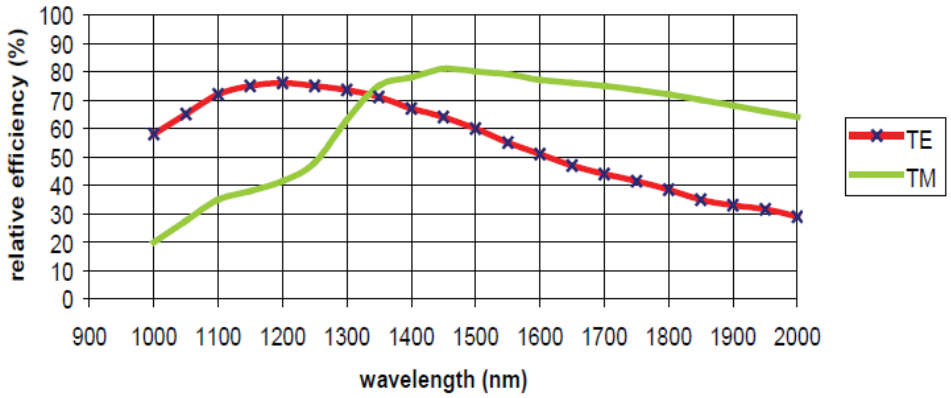

Figure 11: Grating Efficiency for the Linear Polarization States (TE and TM). [15]

The Horiba Symphony II CCD detector consists of a 1024 element array of 25x500 µm pixels. Each pixel covers a spectral range of about 0.05 nm. Incident photons are converted to electrons, and measured as counts. The detector is cooled to -103°C with liquid nitrogen to reduce thermal noise. The quantum efficiency is about 85% from 1000nm to 1600nm. The high dynamic range gain is 1545 e^-/count, and the high sensitivity gain is 58 e^-/count. Because of thermally generated electrons, there is a non-zero signal even when no input is applied. This "dark signal" is recorded and subtracted from future measurements. Counts can be converted to power by the following expression:

$$P[\lambda] = \frac{Counts[\lambda] - Dark[\lambda]}{dT} * \frac{G}{\eta_d} * \frac{hc}{\lambda}$$

Where the measured counts and dark signal are expressed as discrete data points. dT is the integration time, or duration of measurement. The first term has units of counts per second, the middle term is photons per count, and the last is energy per photon. The total power between two wavelengths is simply:

$$P_{\lambda_{12}} = \sum_{\lambda_1}^{\lambda_2} P[\lambda]$$

An example dark signal using 10 second integration is shown in Figure 12 below. Since the scan range is over several hundred nanometers, multiple frames are "stitched" together to create the

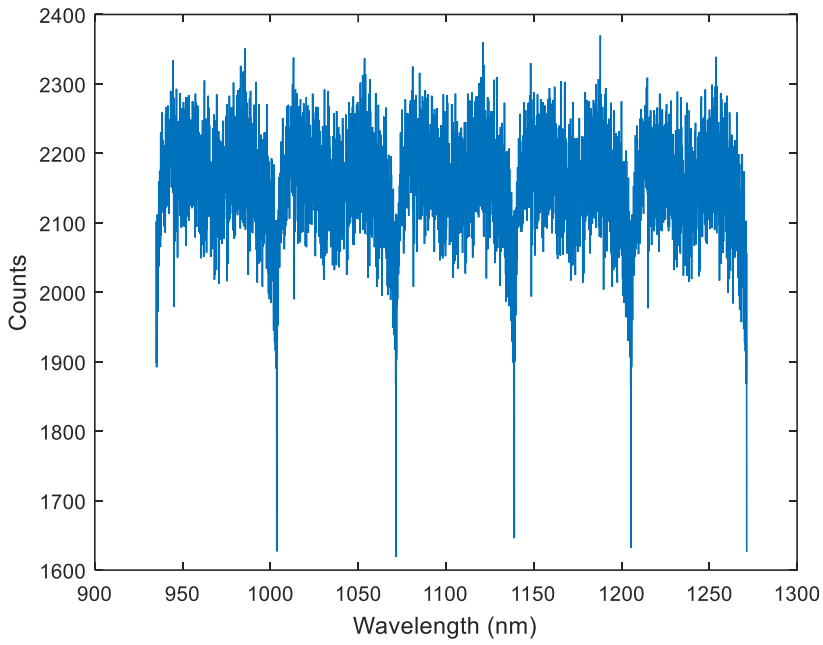

Figure 12: 10 Second Dark Signal

complete spectrum. Due to variations in the pixel fabrication process, and the random thermal generation, the signal is not flat. A pixel overlap is often employed to smooth out the frame transitions, typically averaging 50 to 100 adjacent pixels together. However in the interest of data fidelity, the overlap is set to 0 pixels.

2.3 Measurement Parameters

A list of all available measurement parameters is given below. Most are set at an optimum value and remain constant between each measurement. Only the laser current and integration time are adjusted regularly. The entrance slit width is set to the smallest distance that doesn't attenuate the signal. The slit height is coarsely adjustable and set at its smallest value of 1 mm.

Measurement Parameters

Parameter	Value or Range
Laser Current	60 mA to 103 mA
Laser Temperature	About 23°C
Entrance Slit Width	0.75 mm
Entrance Slit Height	1.0 mm
Grating	600 G/mm at 1500nm blaze
CCD Gain	High Sensitivity (58 e^-/count)
CCD Read Speed	300 kHz
CCD Pixel Overlap	0
Integration Time	1 s to120 s typical

3. System Calibration

3.1 Alignment

The high sensitivity demand combined with the fiber coupled output makes the system extremely sensitive to alignment errors. Considering the excitation and emission optical paths, there are four possible alignment cases depicted in Figure 13.

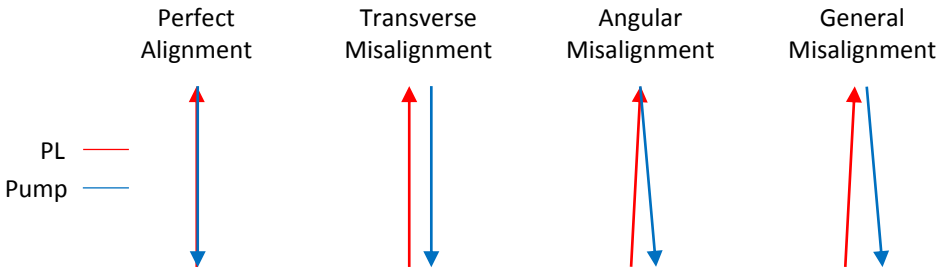

Figure 13: Misalignment Cases

To bring the two paths into alignment, a multi-step process is used. First, a photo detector is placed at the sample position using the XYZ stage, and an infrared laser tunable from 1460nm to 1580nm is connected to the output collimator as shown in Figure 15. The photo detectors in the lab cover either the visible, or IR spectrum. Each beam must be independently aligned to its respective detector. However the two detectors are not likely to be in the same position for each procedure, so only coarse alignment is achieved.

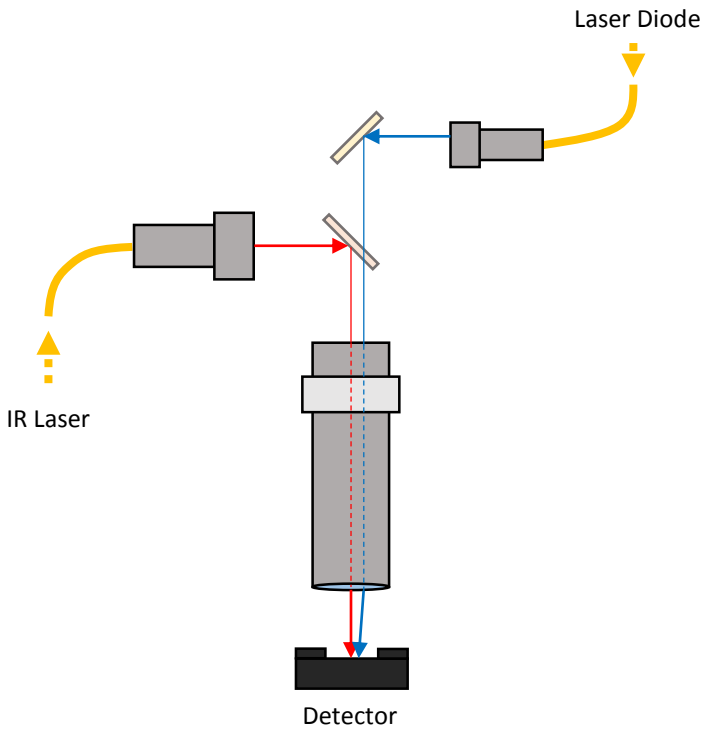

Figure 15: Alignment Setup 1

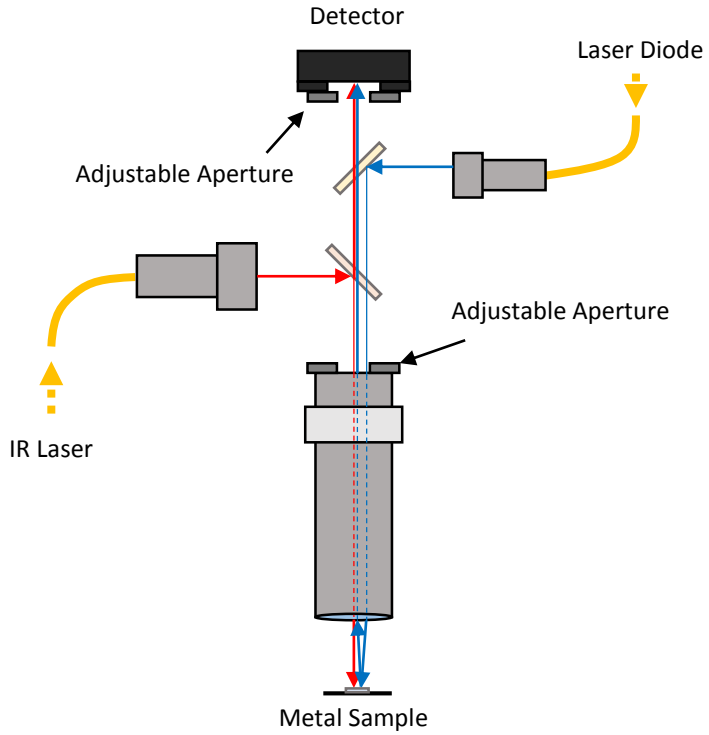

Figure 15: Alignment Setup 2

The second alignment step is to replace the digital microscope with an adjustable aperture and detector as shown in Figure 15. The aperture diameters can be adjusted from 12 mm to 0.8 mm. An aluminum coated sample with high reflectivity is used. The small amount of light transmitted through the dichroic mirrors is well above the detector's noise floor. The alignment controls are adjusted to provide maximum power, then both apertures are reduced until the power drops noticeably. The process is repeated until further improvement cannot be achieved. Similar to the first step, each beam is aligned to its corresponding detector. However, the detectors are now physically mounted to the PL system, and are in nearly the same position. Forcing the beams to pass through both apertures allows the user to adjust the controls until the beams are nearly collinear.

The third alignment step is to adjust the monochromator entrance optics. Using the standard setup in Figure 3, the monochromator is programed to scan at 642nm, the pump wavelength. The position of the input fiber, and two lenses depicted in Figure 10 are adjusted until maximum power is achieved. The last step is fine adjustment of the dichroic mirrors while measuring PL from the surface of a bare silicon wafer. Once the maximum PL signal is achieved, the system is considered to be in alignment, and is ready for measurements.

3.2 Characterization

3.2.1 Infrared Laser Transmission Tests

The system collection efficiency is characterized using the tunable IR laser and measuring the power loss throughout the system.

- Test 1: Output Collimator to Sample

The IR laser is connected via fiber to the output collimator and focused onto the photo detector which is placed at the sample position. The setup and measured loss are shown in Figure 16 below. The input power was -30dBm. The measured loss is approximately 6.2 ± 1 dB. The loss is due to fiber coupling to the collimator, transmission through the collimator lenses, reflection of the mirror, transmission through the objective, and the responsivity of the detector. This can be expressed is the loss term L_0. Then the output power is simply:

$$P_{out1} = P_{in} - L_0$$

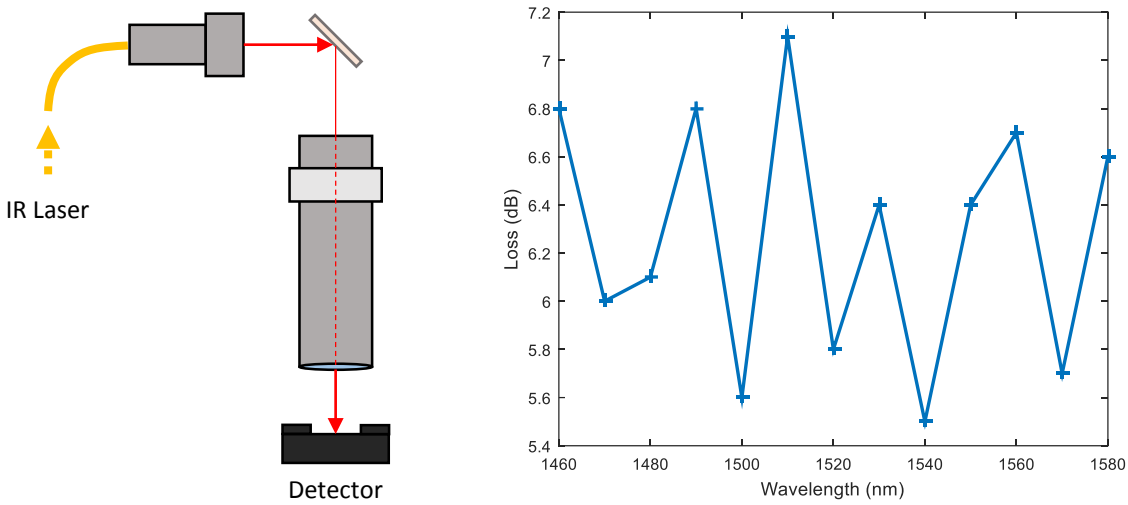

Figure 16: (Left) Test 1 Setup. (Right) Measured Loss from Collimator to Sample

- Test 2: Sample to Monochromator Entrance

The IR laser is placed at the sample position using a lensed fiber adapter. The system is obviously not optimized for collecting emission from a laser, so only a fraction of the light is coupled into the output fiber. Instead of connecting the fiber to the monochromator, it is connected to the same detector used in test 1. The goal is to characterize what fraction of the laser light is actually coupled to the fiber. This is used in test 3 to characterize the entire system. The laser light will experience the same losses from test 1, but there is an additional field of view loss describing how much of the light is coupled into the fiber. This can be written as:

$$P_{out2} = P_{in} - L_0 - L_{fov}$$

Where L_{fov} is the field of view loss. Then using the results from test 1:

$$P_{out1} - P_{out2} = L_{fov}$$

The setup and measured loss are shown below in Figure 17.

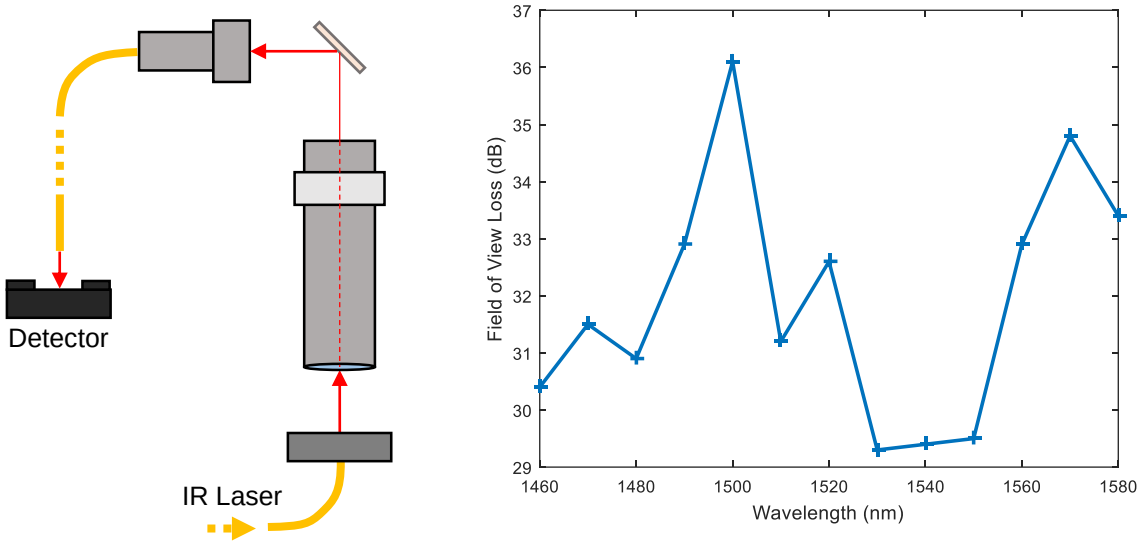

Figure 17: (Left) Test 2 setup. (Right) Measured Field of View Loss

- Test 3: Sample to CCD

The output fiber is now connected to the monochromator so the laser light can propagate through the entire system and reach the CCD. The spectra in Figure 18 below were collected using a 10 ms integration time, and the total power was calculated as described in section 2.2.6 above.

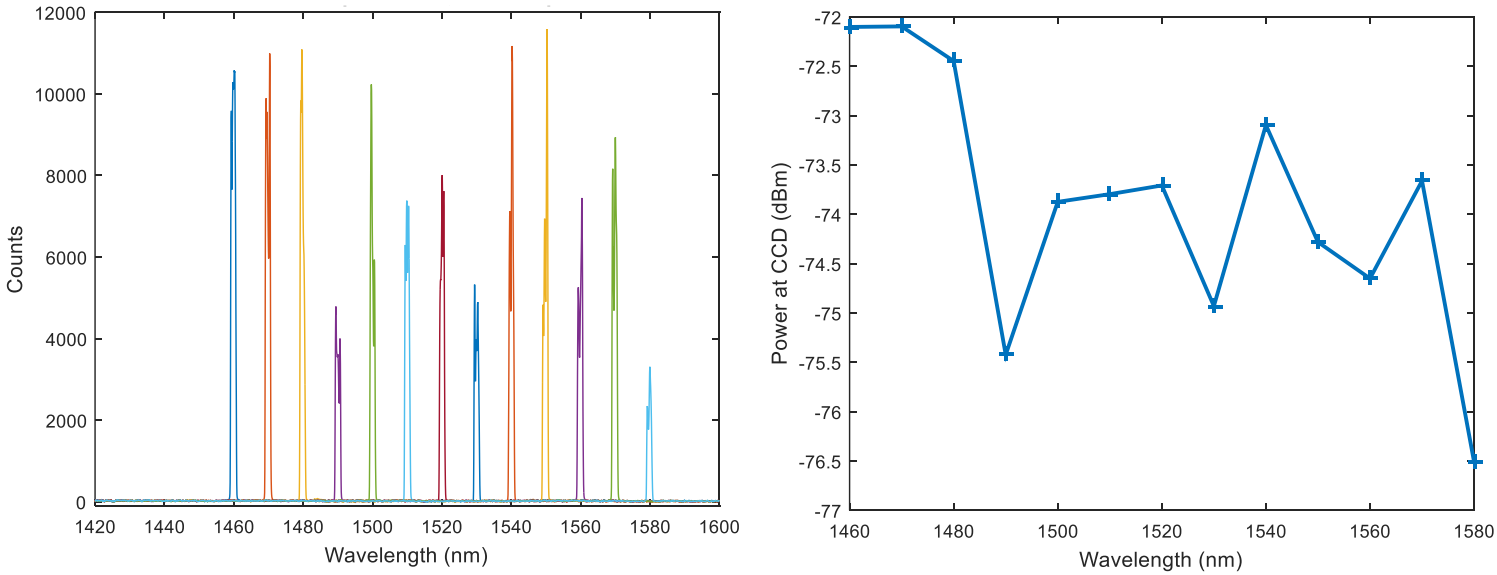

Figure 18: (Left) Spectra of the IR Laser. (Right) Total Laser Power Reaching the CCD

The total loss calculated from the three test results is given in Figure 19. The average system loss is 13 dB, and includes the transmission coefficient of all optical elements. However it does not account for the NA of the objective, i.e. the percentage of light emitted by a PL sample that is actually collected. Test 2 does not account for this because the radiation pattern of the laser is much different than a PL sample which is assumed to be isotropic.

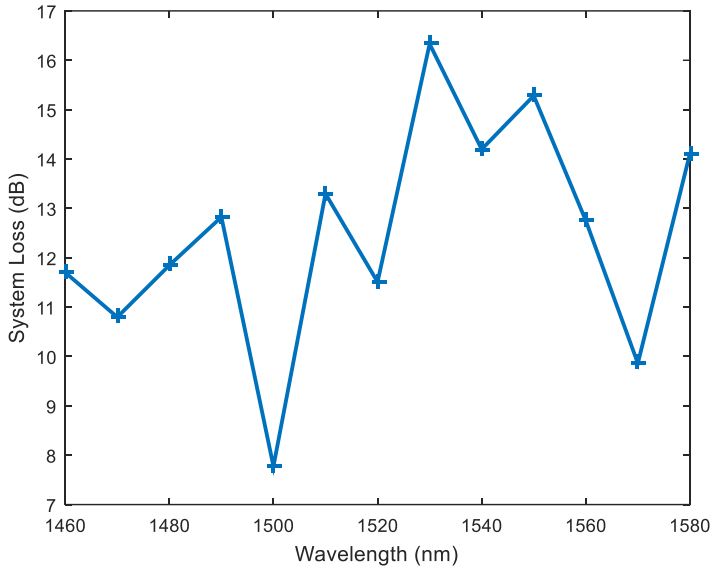

Figure 19: Measured System Loss

3.2.2 Calculation of Light Collection Efficiency

Since the photon energy of the incident laser light is greater than the bandgap energy, free carriers are generated in the silicon. If one electron-hole pair is generated per photon, then the generation rate is given by [9]:

$$G(z) = \alpha\Phi_0(1-\Gamma)e^{-\alpha x} \qquad carriers/cm^3 s$$

Where $(1-\Gamma)$ accounts for reflection at the surface/air interface, and α is the material absorption coefficient. Excited carriers can recombine through multiple processes, if a photon is generated, it is called a radiative process. A figure of merit is the internal quantum efficiency:

$$\eta_i = \frac{R_r}{R}$$

Here R_r is the radiative recombination rate, and R is the total recombination rate, including the non-radiative processes. Once a photon has been emitted within the material, one considers the external quantum efficiency η_e which is the likelihood that the photon is collected by the objective. As depicted in Figure 20 below, only a small fraction of light will be emitted into the objective's field of view.

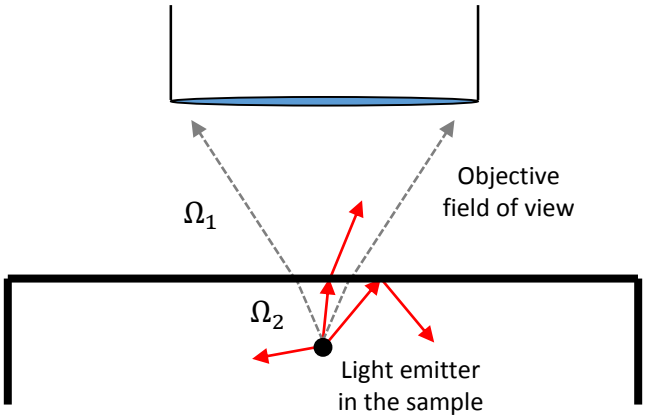

Figure 20: Radiating Point in the Sample. Solid Angles Ω_1 and Ω_2 Describe Acceptance Cone of the Objective

Light emitted towards the objective still experiences losses from re-absorption, and surface reflections. Since the PL is expected to be sub-bandgap and near the surface, absorption can be ignored. Thus the rate of photons entering the objective's field of view is expressed as:

$$I = \frac{\Omega_2}{4\pi}(1-\Gamma) * R_r = \eta_e * R_r = \eta_e * \eta_i * R \quad photons/s$$

Here Ω_2 is the internal solid angle subtended by the radiating point, and 4π is the solid angle of a sphere. For an isotropic radiator, $\Omega_2/4\pi$ is the fraction of photons emitted in the objective's field of view. Γ is the reflection coefficient of the surface/air boundary.

The NA of the objective is not reported in the specification documents, but it can be estimated from the dimensions. The measured lens radius is 11.25 mm, and the specified working distance is 15 mm. Typical 10x objectives with a 15 mm working distance have a slightly longer 20 mm focal length. The clear aperture is the useable part of the lens and is approximately 90% of the diameter. The NA is approximated as:

$$\theta_1 = \tan^{-1}\left(\frac{r * .9}{f}\right) = \tan^{-1}\left(\frac{10.1}{20}\right) = 26.9°, \text{ then } NA = n_1 \sin(\theta_1) = 1 * \sin(26.9°) = 0.45$$

However not all of the light collected by the objective is coupled into the fiber. The principal of geometric extent says that:

$$G_1 = A_1\Omega_1 = A_2\Omega_2 = G_2$$

Where $A_1, \Omega_1, A_2, \Omega_2$ are the area and subtended solid angle of a source and an image respectively. The quantity G is called the geometric extent. The output fiber has a much smaller area than any other optic in the system, which makes it the limiting element. The fiber dimeter is 62.5 μm, and the NA is 0.275. Then the acceptance angle and solid angle are found by [10]:

$$\theta_{\text{fiber}} = \sin^{-1}(0.275) = 15.96°, \quad \Omega_{fiber} = 2\pi(1 - \cos(15.96°)) = 0.2423$$

If the emitting area is approximated as equal to the laser spot area and assumed to radiate in all directions, then the fraction of light collected is roughly given by:

$$\eta_e = \frac{G_{fiber}}{G_{source}}$$

The laser spot size on the sample surface was measured as 35 μm using the method described in section 3.2.3 below. Then the efficiency is:

$$\eta_e = \frac{\pi\left(\frac{62.5}{2}\ \mu\text{m}\right)^2 * 0.2423}{\pi(35\ \mu\text{m})^2 * 4\pi} = 0.0154$$

Which corresponds to 18 dB loss from light not being coupled into the fiber.

3.2.3 Calculation of Incident Power Density

The pump laser is expected to have a Gaussian profile. The intensity of a Gaussian beam propagating along the z-axis is given by [11]:

$$I(r,z) = I_0\left(\frac{\omega_0}{\omega(z)}\right)^2 e^{-\frac{2r^2}{\omega^2(z)}}$$

where I_0 is the initial intensity, and $\omega(z)$ is the spot size, with $\omega_0 = \omega(0)$. As the beam propagates, the spot size varries by:

$$\omega^2(z) = \omega_0^2\left[1 + \left(\frac{\lambda z}{\pi\omega_0^2 n}\right)^2\right]$$

Where λ is laser wavelength and n is material refractive index. Thus when $r = \omega(z)$, the intensity is $1/e^2$ of its max value. A Gaussian beam profile is depicted in Figure 21 below.

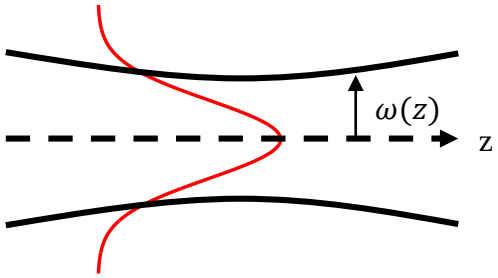

Figure 21: Gaussian Beam Propagation

An optical system can be characterized by a transfer matrix:

$$M_{system} = M_n M_{n-1} \dots M_2 M_1 = \begin{pmatrix} A & B \\ C & D \end{pmatrix}$$

Where M_1 to M_n are transfer matrices for the optical elements in the system. The propagation of a Gaussian beam can be described by initial and final beam parameters q_i, q_f and the coefficients of the transfer matrix in the following expression:

$$q_f = \frac{Aq_i + B}{Cq_i + D}, \qquad where \frac{1}{q} = \frac{1}{R} - j\frac{\lambda}{\pi\omega^2 n}$$

R is the radius of curvature of the beam. The final beam spot size is given by solving for ω.

$$\omega_f = \sqrt{\frac{\lambda}{-\pi * Im\left\{\frac{1}{q_f}\right\}}}$$

To simplify the analysis, it is assumed that all of the power is contained in a circle of radius ω. Then the incident power density at the sample surface is given by the following expression:

$$\Phi_0 = T\frac{P}{\pi\omega_f^2} \quad W/cm^2$$

Where T is the transmission coefficient for the system optics accounting for losses, and P is laser output power. Figure 22 shows the imaged laser spot and a two term Gaussian fit used to extract the spot size as 35 µm.

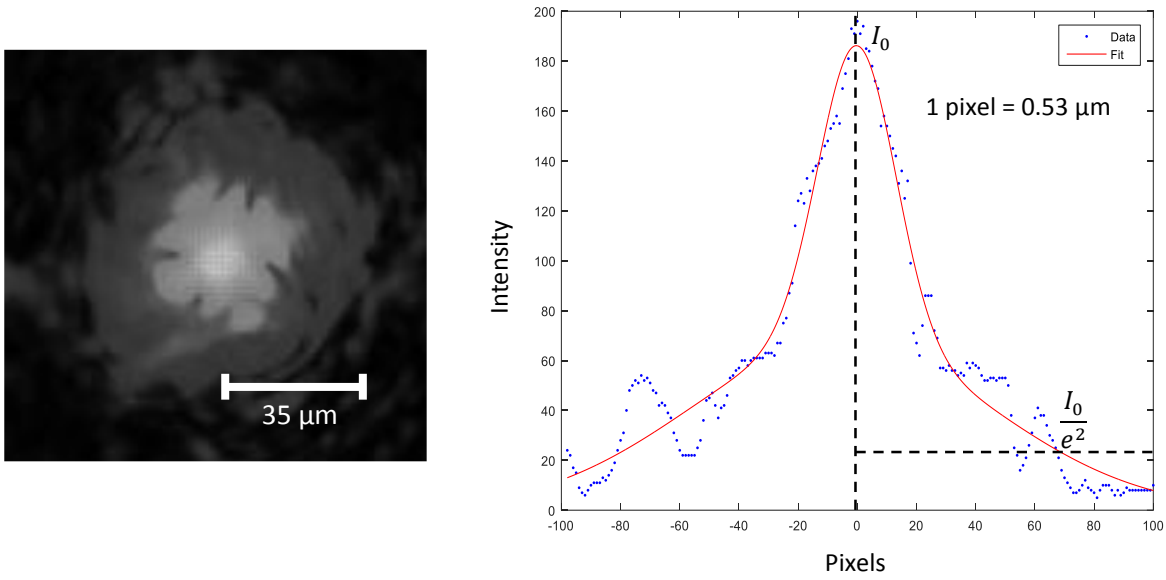

Figure 22: (Left) Imaged Laser Spot. (Right) Two Term Gaussian Fit to Image Intensity

Scattering due to surface and system imperfections will causes the spot to appear larger than it is. Thus 35 µm is an upper limit for the spot size. The transmission coefficient is found by multiplying the coefficients of the individual optical elements. The transmission is near 100% except for the DMSP1000 dichroic mirror which has 91% transmission at 642nm. The corresponding incident power density is:

$$\Phi_0 = 0.91\frac{.02}{\pi\,(35\ \mu\text{m})^2} = 473 \quad W/cm^2$$

3.2.4 Sources of Noise

When extreme sensitivity is required, unwanted noise is an important concern. There are four common noise sources in photo detection: signal shot noise, background radiation, detector thermal noise, and detector read noise. Adding an excitation pump such as a laser can also introduce unwanted signals.

Signal shot noise is associated with detecting the desired PL signal. At the detector, the arrival of each photon is statistically independent from the others. If on average $\bar{n}$ photons are observed in a time interval Δt, then the probability of detecting n photons during Δt is given by the Poisson distribution [12]:

$$P(n|\bar{n}) = e^{-n}\frac{\bar{n}^n}{n!}$$

The standard deviation of the Poisson distribution is $\sigma_n = \sqrt{\bar{n}}$. The signal to noise ratio (SNR) is then calculated as:

$$SNR = \frac{\bar{n}}{\sqrt{\bar{n}}} = \sqrt{\bar{n}} = \sqrt{\bar{r}\Delta t}$$

Where $\bar{r}$ is the average rate of photon arrival. Thus a longer observation time will improve the SNR. Background radiation comes from ambient energy in the environment, and is minimized by lowering the ambient temperature. Thermal noise is due to electrons being excited by thermal energy within the CCD, which is minimized via liquid nitrogen cooling. Both signals follow the same Poisson distribution as shot noise. Detector read noise includes any noise from the circuits used to read the charge on the detector such as amplifiers, analog to digital converters (ADC), etc. Read noise can be reduced by using the slowest ADC speed settings, and decreasing ambient temperature. In practice, the thermal noise is dominant. Measurements are conducted by first measuring the dark signal as discussed in section 2.2.6, then measuring a spectrum with the laser on and subtracting the dark signal to produce an adjusted signal. The SNR is then given by:

$$SNR = \frac{\bar{n}_{adj}}{\sigma_{adj}} = \frac{\bar{r}_{PL}\Delta t}{\sqrt{\bar{r}_{PL}\Delta t + 2\left(\bar{r}_{bg}\Delta t + \bar{r}_{thm}\Delta t + \sigma_{read}^2\right)}} = \frac{\bar{r}_{PL}\sqrt{\Delta t}}{\sqrt{\bar{r}_{PL} + 2\left(\bar{r}_{bg} + \bar{r}_{thm} + \frac{\sigma_{read}^2}{\Delta t}\right)}}$$

Where $\bar{r}_{PL}$, $\bar{r}_{bg}$, and $\bar{r}_{thm}$ are the rates of photoluminescence, background radiation, and thermal excitations respectively. σ_{read} is the standard deviation of the read noise, and Δt is the exposure time. The factor of 2 in the denominator appears because when the dark signal is subtracted, all of the variances add. The most direct way to improve SNR is to increase the exposure time. However if the exposure time is too long, the total number of counts can exceed the CCD full well capacity (~85,000 counts in High Gain mode).

Reflected laser light can add noise, and even damage the sensitive detector. An example laser spectrum is shown in Figure 24. The power concentrated at the laser line can easily saturate measurements. Additionally, amplified spontaneous emission (ASE) noise generated far from the

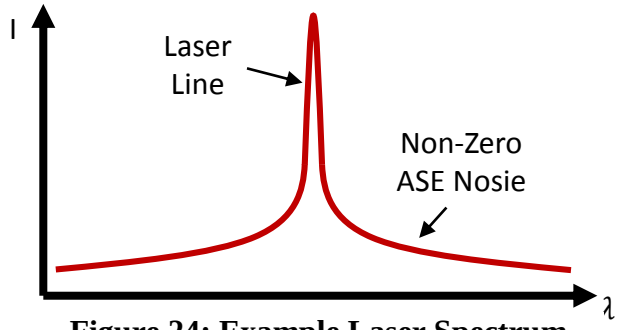

Figure 24: Example Laser Spectrum

laser's center wavelength can completely suppress the desired PL signal. Optical spectrum analyzer (OSA) measurements were conducted with the help of Justin Burr. He found the proper resolution bandwidth (RBW) and sensitivity settings for measuring the laser's spectral characteristics. The laser spectrum was measured from 635nm to 645nm, and from 1400 nm to 1600 nm. The results are shown in Figure 23. ASE is clearly present from past 1400 nm, which is the desired PL measurement range. Both the laser line and ASE noise need to be suppressed by optical filters as discussed in section 2.2.4.

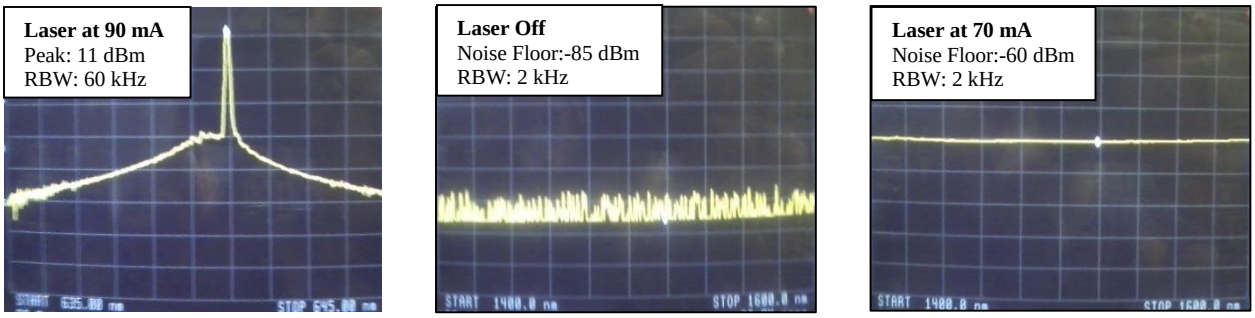

Figure 23: (Left) Laser Line Spectrum. (Middle) Near IR Spectrum – Laser Off. (Right) Near IR Spectrum – Laser On.

4. Measurements and Discussion

4.1 Laser Noise and Ghosting

As discussed in section 2.2.4, high performance optical filters are necessary to sufficiently attenuate the pump source. Figure 25 and Figure 26 were taken without the upgraded filters. Figure 25 shows both the fundamental and second order diffraction peaks. Even at moderate drive current and integration times, scanning over the laser line will immediately saturate the detector.

In Figure 26 peculiar artifacts known as grating ghosts [8] are present. Manufacturing defects cause the laser light to be scattered into unwanted directions, contaminating the sensitive PL measurement. With the high performance filters, the ghosts are completely suppressed because the laser power is significantly attenuated.

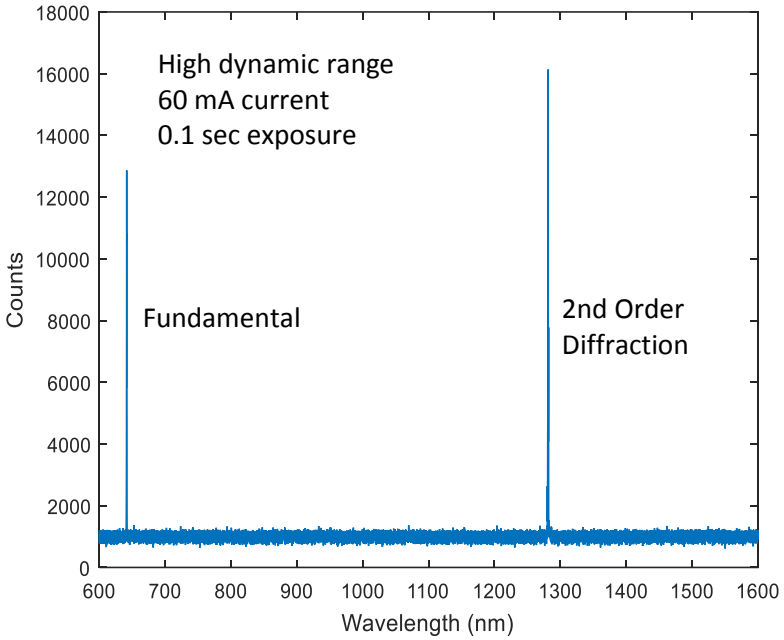

Figure 25: Fundamental and Second Order Diffraction of Laser Light

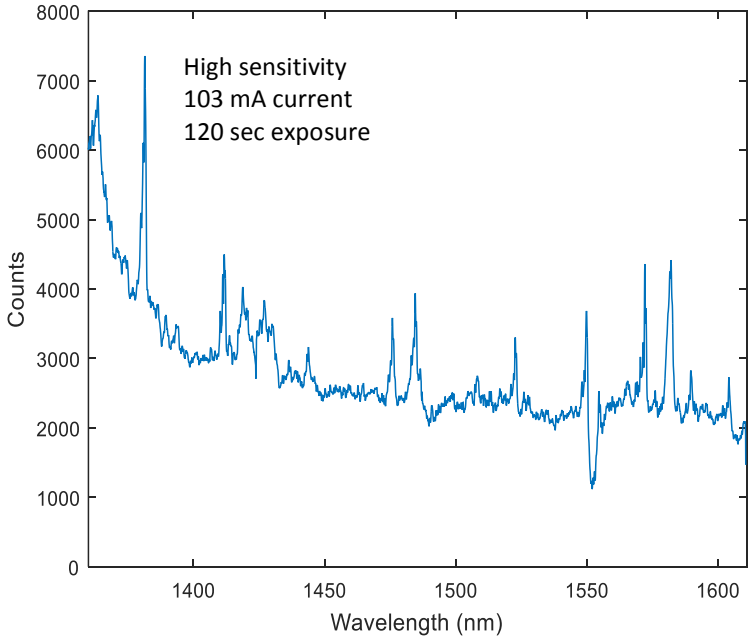

Figure 26: Grating Ghosts

4.2 Signal Processing

Figure 27 below shows unprocessed PL data from a bare Czochralski (CZ) silicon sample with 103 mA laser current and variable integration time. The peak is band-edge luminescence of silicon, i.e. the inefficient phonon assisted process depicted in Figure 1. Both the noise, and SNR clearly increase with measurement time.

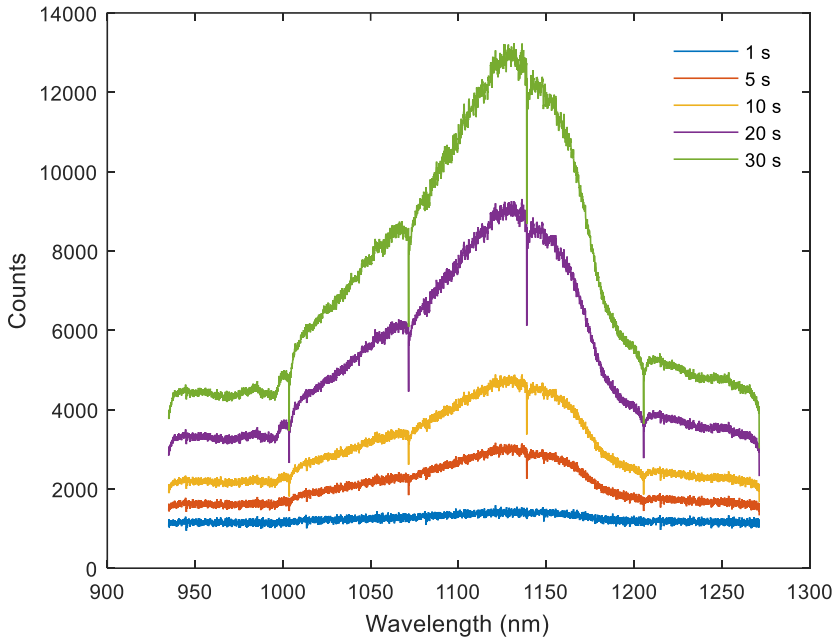

Figure 27: Silicon Band-Edge PL with Variable Integration Time

A plot of the 30 second measurement after subtracting the dark signal is shown in Figure 28 below. There are noticeable jumps in the signal at the frame boundaries. The one at 1125nm is nearly 1000 counts. This is due to variations in quantum efficiency across the detector. To measure the detector response, a small wavelength range was scanned across the detector such that a nearly constant signal was exposed to each pixel. The results shown in Figure 29, reveal that the response increases almost linearly. This explains why there is a drop from high to low between each frame. The response data is used in conjunction with a five point moving average filter to process the measurement. The 30 second measurement with post processing is shown in Figure 30.

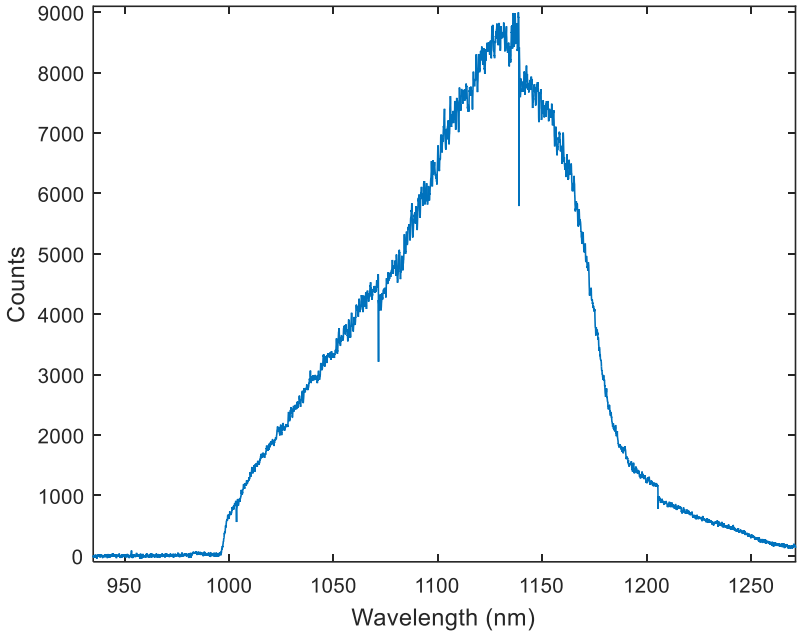

Figure 28: Silicon Band-Edge PL with 30 s Integration at 103 mA

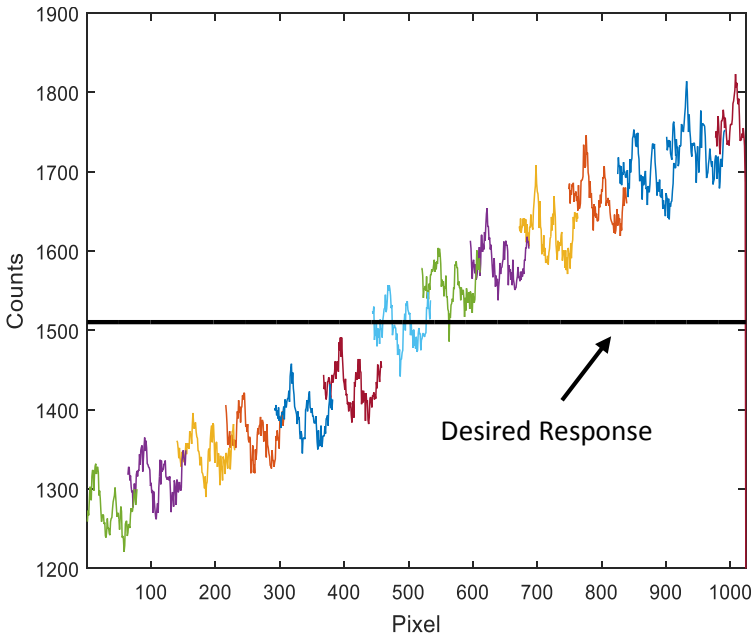

Figure 29: Measured Detector Response

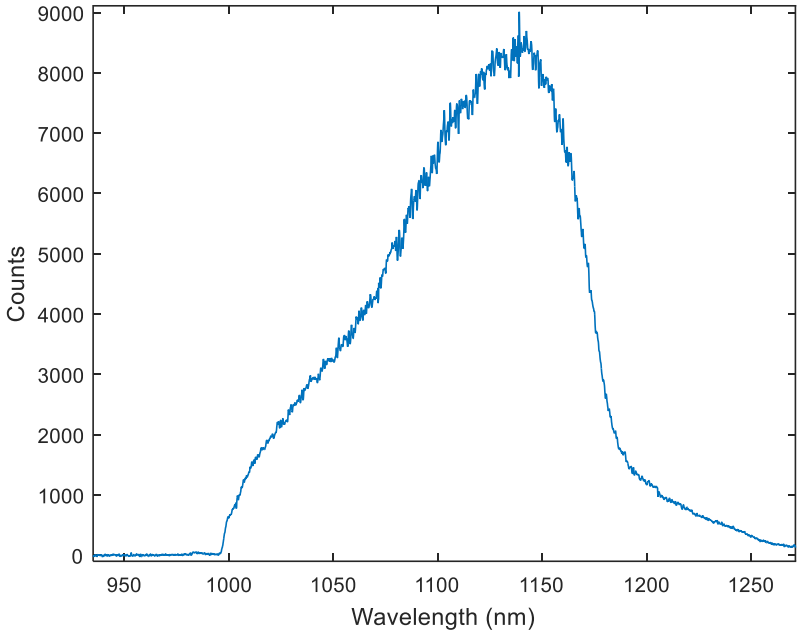

Figure 30: Silicon Band-PL after Data Correction

4.3 Grating Comparison

As discussed in section 2.2.6, the monochromator is equipped with three gratings. Figure 31 below shows band-edge PL measured with each of the gratings using 103 mA laser current and 10 second integration time. As expected, grating 3 has the greatest SNR because of the lower groove density. The blaze wavelength of grating 2 is closer to the PL signal than the blaze wavelength of grating 1 which means grating 2 is slightly more efficient. The total spectral power for each curve is calculated all three curves is reported below.

Total Measured Power

Grating	Power (pW)	Power (dBm)
1	5.9	-82.3
2	6.6	-81.8
3	5.9	-82.3

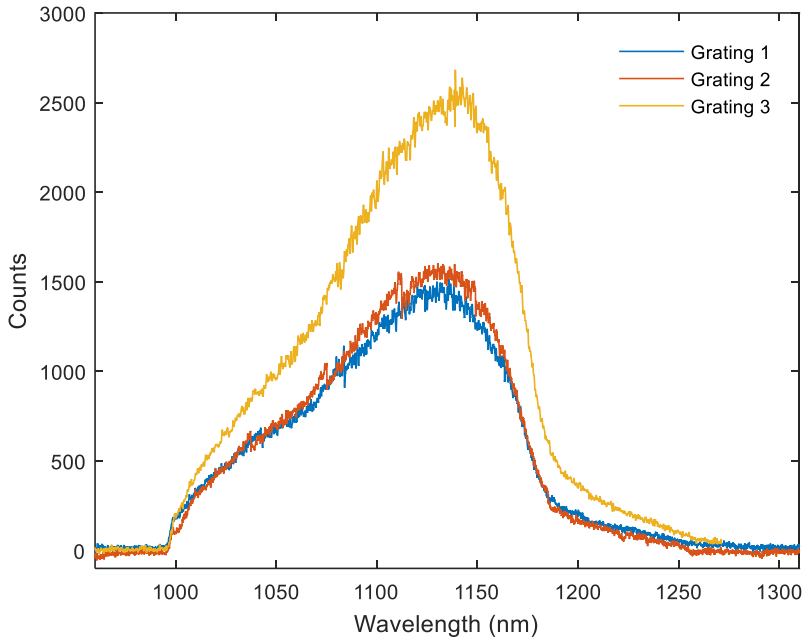

Figure 31: Silicon Band-Edge PL vs Grating

The total power is nearly equal for each curve as expected. Even though the intensity is lower for gratings 1 and 2 there is a greater number of data points due to the increased resolution which yields the same total power. Using the characterization results from section 3.2, the power emitted can be estimated as:

$$P_e = P_m + L_{sys} + L_G = -82.3 + 13 + 18 = -51.3 \text{ dBm} = 7.4 \text{ nW}$$

Where P_m is the measured power at the detector using grating 3, L_{sys} is system loss, and L_G is loss from the geometric extent. The incident laser power is about 20 mW. Using the approximation that all of the laser power is converted to carriers, the internal quantum efficiency is:

$$\eta_i = \frac{7.4 \text{ nW}}{20 \text{ mW}} = 3.7 * 10^{-7}$$

While this is an under estimate because of the laser power approximation, it is the proper order of magnitude range for silicon internal quantum efficiency. Accounting for lost laser power will increase the calculated efficiency.

4.4 Sub-Bandgap Photoluminescence from SOI

Silicon on insulator (SOI) wafers were purchased from Soitec with a 340 nm top silicon layer and 1 µm buried oxide. Michael Wood prepared the samples for plasma treatment by thinning the top

Si layer from 340nm to 250nm, which is a common device layer thickness. Then he treated the surface with hydrogen plasma as depicted in Figure 32. The measured PL spectra are shown in Figure 33. All three treatments produced sub-bandgap PL around 1300nm.

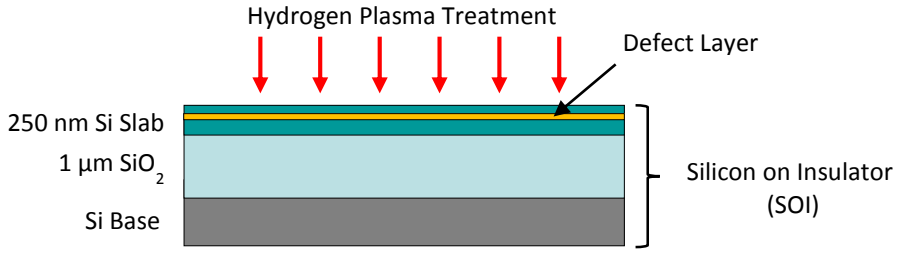

Figure 32: SOI Sample with Hydrogen Plasma Treatment

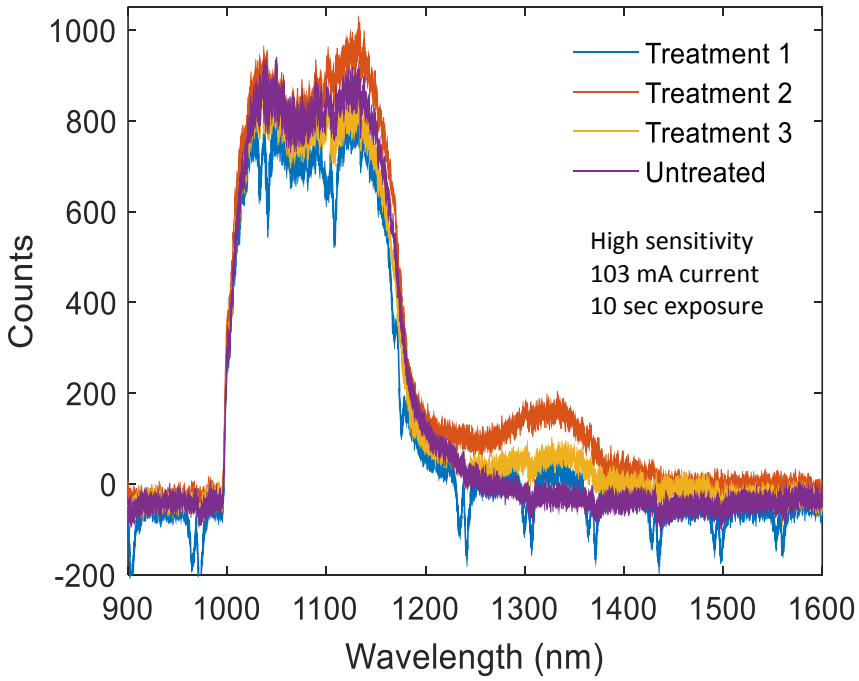

Figure 33: SOI Sub-Bandgap PL Comparison

Examining the literature, the sub-bandgap PL was expected to be stronger. The hydrogen plasma treatment was similar to that in [13] which reported the PL in Figure 34 below.

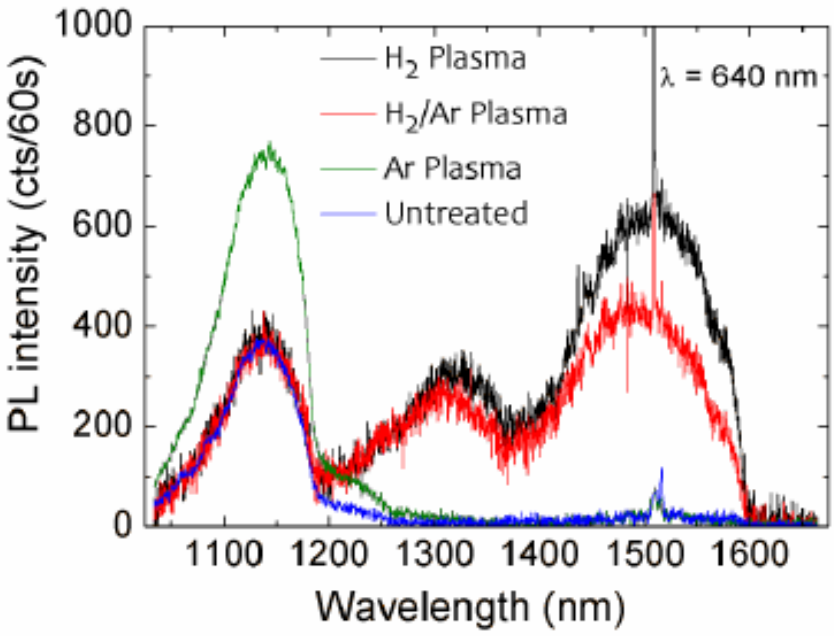

Figure 34: PL from hydrogen plasma treated SOI reported in [13]

Without detailed knowledge of the detection setup used, it is difficult to directly compare the two measurements. However hydrogen plasma treatment clearly resulted in two peaks at 1300 nm and 1500 nm with an intensity comparable to the band-edge peak at 1100 nm. Careful control of the fabrication parameters is likely required to produce intensities similar to [13]. Investigating why the spectral shape of the band-edge peak is different may also provide insight into optimizing the sub-bandgap signal. Michael Wood can use these results to adjust the fabrication process for the next set of samples.

6. Conclusion

Silicon light emission is an active research area because of the need for a native on chip silicon light emitter. Sub-bandgap emission is particularly attractive because it is not prone to re-absorption. Recent research has investigated optically active defects that emit at sub-bandgap wavelengths. The extremely low power of the emitted light poses a unique challenge. A custom photoluminescence system has been designed, built, and demonstrated for detecting sub-bandgap photoluminescence in silicon. A free-space optical system was designed to couple laser energy to the sample surface, and to couple photoluminescence to the detector. A digital microscope was incorporated to provide video feedback of the sample surface. The design includes high precision mechanical stages and multiple detectors which are used to align the optics in an iterative

procedure. Photoluminescence was measured from research level samples and compared with current literature. The results can be used to motivate the next stage of research.

7. Future Work

The system can be improved in two areas. The first is increased sensitivity, the second is increased functionality. The sensitivity is a function of the SNR, and there is no avenue to significantly reducing the noise other than finding a lower temperature detector. The collected signal power depends on the excitation power, and the overall collection efficiency. A more powerful laser would increase the measured signal, but there are limits of heat dissipation, and available number of radiative states. The collection efficiency can be increased by using optics with higher transmittance and reflectance, and by maximizing the geometric extent. The small area of the fiber is currently limiting the geometric extent. A larger diameter, and larger NA fiber would be able to collect more light, but would also require a new set of collimating lenses. Another alternative is to remove the fiber and couple directly into the monochromator. The disadvantage of this approach is that the output couldn't be analyzed with other lab equipment, the monochromator would be dedicated to this experiment only, and stray light would be much more problematic because of the free-space coupling. The system functionality can be expanded by enabling different types of measurements. Incorporating electrical probes would allow electroluminescence measurements on electrically pumped devices. The probes would simply need to be small enough to fit between the sample and objective lens. Adding a lock-in amplifier and optical chopper would enable pulsed excitation and time-resolved measurements. The main difficulty would be synchronizing the lock-in with the monochromator and CCD detector through software. A cryostat could be used for low temperature measurements, but would be difficult to incorporate into the current setup because of the limited space around and below the objective. Improving both the system sensitivity and its functionality would enable further research in sub-bandgap silicon luminescence.

8. References

[1] P. M. Fauchet, "Monolithic Silicon Light Sources," in *Silicon Photonics, Volume 1*, L. Pavesi and D. J. Lockwood, Eds., Springer, 2004.

[2] A. Shakoor, R. L. Savio, S. Portalupi and e. al., "Enhancement of room temperature sub-bandgap light emission from silicon photonic crystal nanocavity by Purcell effect," *Physica B*, vol. 407, pp. 4027-4031, 2012.

[3] T. H. Gfroerer, "Photoluminescence in Analysis of Surfaces and Interfaces," *Encyclopdia of Analytical Chemistry,* pp. 9209-9231, 2000.

[4] I. Sychugov, R. Juhasz, G. A., J. Valenta and J. Linnros, "Single dot optical spectroscopy of silicon nanocrystals: low temperature measurements," *Optical Materials,* vol. 27, pp. 973-976, 2005.

[5] M. Galli, S. L. Portalupi, M. Belotti, L. C. Andreani, L. O'Faolain and T. F. Krauss, "Light scattering and Fano resonances in high-Q photonic crystal nanocavities," *AIP*, no. 94, 071101, 2009.

[6] OSHA, *OSHA Technical Manual Section III: Chapter 6 Laser Hazards,* 2015.

[7] Horiba Scientific, *Gratings - Instrument Performance Report,* 2014.

[8] Horiba Scientific, *Diffraction Gratings Ruled & Holographic,* 2015.

[9] D. A. Neamen, "Ch.14 Optical Devices," in *Semiconductor Physics and Devices*, 2012, pp. 618-628.

[10] O. Mazonka, "Solid Angle of Conical Surfaces, Polyhedral Cones, and Intersecting Spherical Caps," *arXiv,* 2012.

[11] J. T. Verdeyen, "Ch. 3 Gaussian Beams," in *Laser Electronics Third Edition*, 2000, pp. 63-80.

[12] B. M. Oliver, "Thermal and Quantum Noise," *Proceedings of the IEEE,* vol. 53, no. 5, pp. 436-454, 1965.

[13] A. Shakoor, "Silicon nanocavity light emitters at 1.3-1.5 um wavelength," *Ph.D. dissertation,* 2013.

[14] Thorlabs, *Fixed Focus Collimation Packages: FC/PC Connectors,* 2015.

[15] Horiba Scientific, *Spectral Efficiency Curve 510 16.*

[16] S. Boninelli, G. Franzo, P. Cardile and a. et., "Hydrogen induced optically-active defects in silicon photonic nanocavities," *Optics Express,* vol. 22, no. 8, 2014.

[17] Thorlabs, "NA Tutorial Numerical Aperture," 2015.

[18] Thorlabs, "Infinity-Corrected Tube Lens," 2015.

Appendix

A. Parts List

Part Number	Vendor	Description	Quantity
LP642-SF20	Thorlabs	Fiber coupled laser diode	1
F280FC-B	Thorlabs	Laser collimator	1
F810APC-1550	Thorlabs	PL collimator	1
GIF625	Thorlabs	Custom output fiber	1
LG7	Thorlabs	Laser safety glasses	2
69204	Edmund Optics	Dichroic mirror	1
DMSP1000	Thorlabs	Dichroic mirror	1
FELH0850	Thorlabs	Longpass filter	2
FESH0800	Thorlabs	Shortpass filter	1
VZM-2000HP	Caltex	Digital microscope	1
iHR550	Horiba	Monochromator	1
Cage Assembly	Thorlabs	System hardware	NA
884-UDAPT	Newport	Mounting adapter	1
818-SL	Newport	Visible Spectrum Detector	1
818-IG	Newport	IR Spectrum Detector	1

Figure 35: Parts List

B. Custom Parts

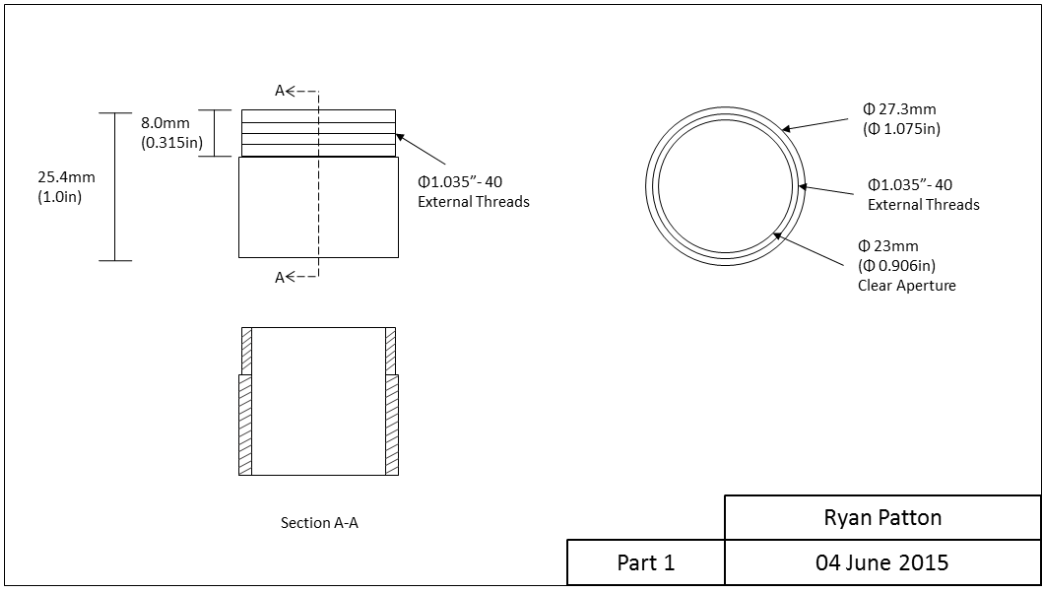

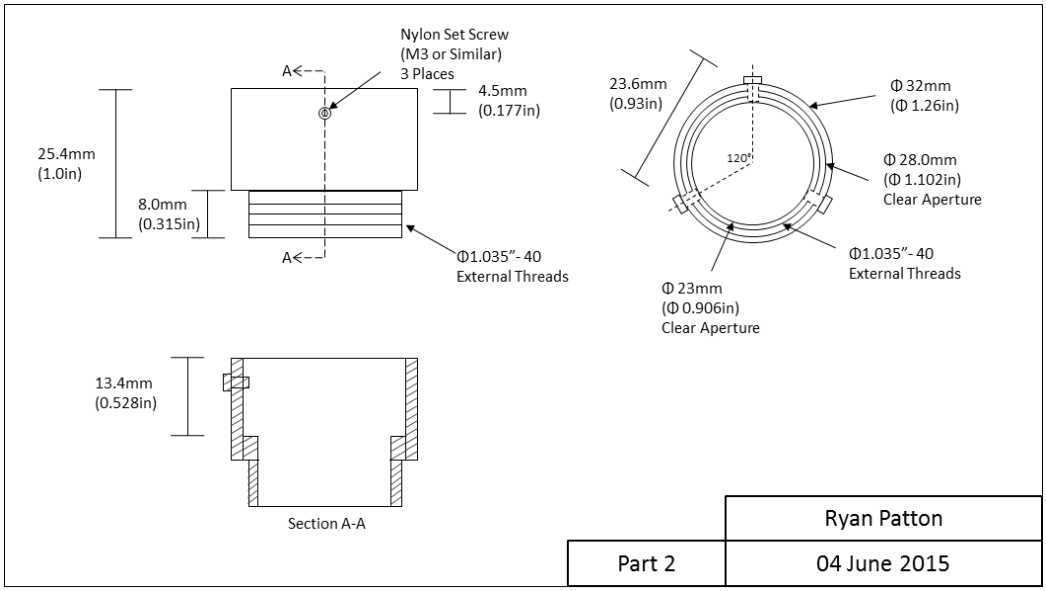
Nylon Set Screw
(M3 or Similar)
3 Places
A
A
4.5mm
(0.177in)
25.4mm
(1.0in)
8.0mm
(0.315in)
Φ1.035”- 40
External Threads
23.6mm
(0.93in)
120°
Φ 32mm
(Φ 1.26in)
Φ 28.0mm
(Φ 1.102in)
Clear Aperture
Φ1.035”- 40
External Threads
Φ 23mm
(Φ 0.906in)
Clear Aperture
13.4mm
(0.528in)
Section A-A
Ryan Patton
Part 2
04 June 2015